Chapter 11

Acousto-optical Scanning-Based High-Speed 3D Two-Photon Imaging In Vivo

Balázs Rózsa, Gergely Szalay, and Gergely Katona

Abstract

Recording of the concerted activity of neuronal assemblies and the dendritic and axonal signal integration of downstream neurons pose different challenges, preferably a single recording system should perform both operations. We present a three-dimensional (3D), high-resolution, fast, acousto-optic two-photon microscope with random-access and continuous trajectory scanning modes reaching a cubic millimeter scan range (now over $950 \times 950 \times 3000\ \mu m^3$) which can be adapted to imaging different spatial scales. The resolution of the system allows simultaneous functional measurements in many fine neuronal processes, even in dendritic spines within a central core ($>290 \times 290 \times 200\ \mu m^3$) of the total scanned volume. Furthermore, the PSF size remained sufficiently low ($PSF_x < 1.9\ \mu m$, $PSF_z < 7.9\ \mu m$) to target individual neuronal somata in the whole scanning volume for simultaneous measurement of activity from hundreds of cells. The system contains new design concepts: it allows the acoustic frequency chirps in the deflectors to be adjusted dynamically to compensate for astigmatism and optical errors; it physically separates the *z*-dimension focusing and lateral scanning functions to optimize the lateral AO scanning range; it involves a custom angular compensation unit to diminish off-axis angular dispersion introduced by the AO deflectors, and it uses a high-NA, wide-field objective and high-bandwidth custom AO deflectors with large apertures. We demonstrate the use of the microscope at different spatial scales by first showing 3D optical recordings of action potential back propagation and dendritic Ca^{2+} spike forward propagation in long dendritic segments in vitro, at near-microsecond temporal resolution. Second, using the same microscope we show volumetric random-access Ca^{2+} imaging of spontaneous and visual stimulation-evoked activity from hundreds of cortical neurons in the visual cortex *in vivo*. The selection of active neurons in a volume that respond to a given stimulus was aided by the real-time data analysis and the 3D interactive visualization accelerated selection of regions of interest.

Key words Two-photon, Acousto-optical, Dendritic imaging, Network imaging, 3D, Three-dimensional microscopy, Angular dispersion compensation, In vivo imaging, Backpropagating action potentials, Temporal super-resolution, Dendritic spikes, 3D scanning, 3D virtual reality environment

1 Introduction

1.1 The Need for 3D Measurements

The systematic understanding of brain function requires methods that allow neuronal activity to be recorded at different spatial scales in three dimensions (3D) at a high temporal resolution. At the single neuron level, activity is differentially distributed in space

Alon Korngreen (ed.), *Advanced Patch-Clamp Analysis for Neuroscientists*, Neuromethods, vol. 113,
DOI 10.1007/978-1-4939-3411-9_11, © Springer Science+Business Media New York 2016

and time across the dendritic and axonal segments [1–6]. Therefore, in order to understand neuronal signal integration, activity should be simultaneously recorded at many spatial locations within the dendritic and axonal tree of a single neuron. At the neuronal circuits level, closely spaced neurons can have vastly different activity patterns [7]; on the other hand, widely separated cells may belong to the same functional circuit, influencing each other via long axonal processes. Therefore, recording techniques are required that collect information near-simultaneously (in one fast measurement sequence) from many cells of a neuronal population situated in an extensive volume of tissue. Moreover, measurements should be possible on the timescales of dendritic integration and regenerative spike propagation [8], i.e., with sub-millisecond temporal resolution. One last aspect is that these measurements should be performed in as intact as possible neurons on neurons or neuronal networks which are as intact as possible, where neurons are embedded in their original tissue. This poses a challenge: cellular precision must be retained in acute brain preparations where the tissue is at least 100-μm thick or, for in vivo experiments, through millimeters of brain material.

1.2 From Wide-Field Microscopy to Single-Point, Two-Photon Excitation

Light microscopy is important in biological research because it enables living tissue to be observed and suited at a relatively high spatial resolution. This resolution is limited by the wavelength of light (according to Abbe's theory) and does not rival that of electron microscopy, but the scope of electron microscopy is limited when observing living specimens [9]. Other vital imaging technologies, such as MRT (magnetic resonance tomography), PET (positron emission tomography), or X-rays, can neither resolve subcellular structures nor provide high temporal resolution nor the exquisite molecular selectivity that would allow single molecules to be detected in a background of billions of others [10, 11].

Light microscopy inside living tissues is hampered by the degradation of resolution and contrast, caused by absorption and light scattering, which is due to refractive index inhomogeneities present to a varying degree in every tissue. Deeper within the tissue, images become more degraded and high-resolution imaging eventually becomes impossible. A major step toward overcoming this problem was the invention of confocal microscopy [12, 13]. In a confocal microscope, the illumination light is focused on a diffraction-limited spot, and this excites the sample along two cones close to the aimed focal point. Then, using the same objective, the emitted signal photons are focused onto a detector pinhole that rejects all light emitted outside of the focus spot.

The main drawback of confocal microscopy is its wasteful use of both excitation and emission. On the one hand, absorption occurs throughout the specimen, but information is obtained only from a small sub-volume around the focal point. On the other hand, light

emitted from the focal point is also rejected by the pinhole if it is scattered by the tissue: this means that tissue scattering has a significant impact on the signal-to-noise ratio (SNR) of the images. This is particularly a major problem in vital fluorescence microscopy, where the limiting factors are usually either photochemical destruction of the fluorophore (photobleaching) or photodynamic damage to the specimen (photodamage). In confocal microscopy, only ballistic photons that are not scattered on their path out of the tissue contribute to the signal, while scattered photons, often the majority, are rejected by the detector aperture, limiting depth penetration of the technology to about 50–80 μm in brain tissue. Excitation needs to be increased in order to compensate for this signal loss which further exacerbates photobleaching and photodamage. All of these problems are general to many other, so-called single photon excitation technologies, among them to the spinning-disc confocal [14] and to the light sheet microscope technologies [15]. Theoretically, these problems can be handled by the use of laser scanning microscopy in combination with two-photon excitation [16, 17].

The concept of two-photon excitation is based on the idea that two photons of low energy can be combined in the same quantum event, resulting in the emission of a fluorescence photon at a higher energy than either one of the two excitatory photons. Although the probability of such absorption is extremely low, its cross section is proportional to the square of the photon flux, making it possible to counterbalance this low initial cross section by using extremely high photon fluxes. Multi-photon absorption is often called nonlinear because the absorption rate is dependent on a higher-than-first-power light intensity. Such high fluxes are only present in the focus of a high numerical aperture lens illuminated by a strong, pulsed near-infrared laser. The possibility of absorbing more than one photon during a single quantum event had been predicted more than 60 years ago [18], but it was confirmed experimentally after the invention of mode-locked lasers with a pulse duration below 1 ps and repetition rates of about 100 MHz. This made two-photon laser scanning microscopy feasible in practice [16].

Mode-locking a Ti:sapphire laser, for example, boosts the two-photon excitation rate by 100,000-fold, compared to continuous-wave (cw) operation at the same average power. On the other hand, the quadratic dependence of the absorption rate on the light intensity gives two-photon microscopy its optical sectioning property because fluorescence is only generated in the vicinity of the geometrical focus where the light intensity is high. While scanning the laser focus in both lateral directions (x and y), fluorescence excitation is limited to the focal plane. No detector pinhole is necessary since—in most cases—no fluorescence is generated outside the focal volume, and all fluorescence photons, whether leaving the sample on scattered or ballistic trajectories, constitute useful signal.

The combination of low phototoxicity enabled by the single-point excitation and the efficient use of fluorescence—even scattered—makes single-point two-photon microscopy a unique tool for observing function deep within the tissue, even resolving structures smaller than 1 mm in brain tissue [19–21]. Its main drawback, however, is speed when compared to camera-based approaches where, instead of the "single-channel" photomultipliers (PMTs), information can potentially be collected from millions of camera pixels simultaneously.

There are several approaches to using multi-site two-photon stimulation in combination with a camera-based detection algorithm to overcome the limitation of single-point illumination. The simplest of these technologies is multi-beam two-photon microscopy [22], where a string of focal spots are generated by breaking the laser beam into parallel beamlets. This causes parallel fluorescent excitation at multiple sites; these are then scanned to illuminate the entire focal plane. Fluorescence is detected by a high-resolution camera after imaging the focal surface onto its sensor chip. This approach makes it possible to image with a higher frame rate than with a scanned single-beam two-photon microscope, but it has one main drawback: imaging florescence onto the camera is sensitive to tissue scattering. As a result, this technology has about the half of the penetration depth of single-point two-photon microscopy and this—especially in the case of in vivo investigations—seriously limits its biological usability.

Recent camera-based approaches can also resolve the 3D structure of a sample by using special light shaping: microlens array [23] or phase mask [24] in front of the camera combined with extended depth of field [25] or holographic [24] illumination. Depth information is obtained from the camera images by computationally reversed transformation, which causes two major limitations. First, there is a strict limit to the number and arrangement of the regions of interest (ROIs) as they should not overlap much on the detector surface. Typically, ROIs situated at the same place but at different depths are imaged to mostly overlapping profiles on the detector surface, making it difficult to distinguish between them. Second, the imaging of the emitted light is sensitive to tissue scattering, causing scattered shapes on the detector surface, challenging the reverse transforming algorithms. For example, Quirin et al. [24] showed penetration depth of about 190 μm (3 × scattering length), which is just enough to reach the first cell layers in mice in vivo, and is much less than the depths achievable by single-point two-photon microscopes.

As we have seen, a single-point illuminated two-photon microscope can reach deep structures with subcellular resolution, which makes this technology the best available tool for functional studies. However, as only one point might be illuminated at a time, special scanning methods need to be developed to sample the important biological features with enough speed to resolve their functionality.

1.3 Why Choose Acousto-optical Scanning for Network and Dendritic Measurements in 3D?

Several novel technologies have been developed to generate 3D readouts of fast population and dendritic activities, including liquid lenses [26], holographic scanning [27], Roller Coaster Scanning [2], piezo-scanning with sinusoidal resonance [28], deformable mirrors, temporal and spatial multiplexing [29], axicon or planar illumination-based imaging [30], fast *z*-scanning based on an axially moving mirror [31], simultaneous multiview light sheet microscopy [15], and optical fiber acousto-optical deflector based 3D scanning [32]. There are three major points why 3D acousto-optical scanning is better than alternative methods:

1. First of all, 3D acousto-optical microscope technology allows single-spot two-photon activation; this permits whole-field detection with high quantum efficiency PMTs. Therefore, photons scattered from deep layers within the tissue can also be collected with a high sensitivity; this is essential for imaging throughout the whole cortex.
2. Moreover, the position of the point spread function (PSF) can be finely adjusted to any spatial coordinates during acousto-optical scanning, with 50–100 nm precision [33]. Therefore, the number of z-planes and coordinates is unlimited, which allows a very precise measurement of neuronal activity by eliminating neuropil contamination.
3. Second, acousto-optical scanning allows flexible selection of regions of interest. Instead of scanning large volumes, we can restrict our measurements only to preselected regions. This subselection increases the product of the measurement speed and the signal collection efficiency by up to several orders of magnitude, as compared to classical raster scanning. More quantitatively, 3D random-access scanning increases the measurement speed and the signal collection efficiency by the following factor:

$$\begin{aligned}&(\text{measurement speed})\,{}^{*}(\text{signal collection})\\&\cong\left(\frac{\text{total image volume}}{\text{volume covered by the scanning points}}\right)\end{aligned}$$

where "signal collection" is defined as the number of fluorescent photons detected in a given time interval from a given spatial location, and the "volume covered by the scanning points" is the convolution of the PSF and the preselected scanning points. In a typical in vivo measurement, using a $450 \times 450 \times 650\ \mu m^3$ scanning volume with a 0.47–1.9 μm and 2.49–7.9 μm axial resolution (see Katona et al. [33]) and simultaneously measuring about 100 locations, *random-access scanning will provide a* 2,106,000–46,534-*fold*, *on average an increase of a six orders of magnitude in the product of measurement speed and signal collection efficiency.* According to the

current state of the technology (which now provides an approximately 1 mm^3 scanning volume with high NA objectives), this increase could be even larger, over 1,000,000,000 per locations. *No other currently available 3D scanning method, with high spatial resolution and deep penetration capability, can provide a similar increase in the product of the measurement speed and the signal collection efficiency.*

2 Principles of Acousto-optical Devices

The phrase "acousto-optic" refers to the field of optics that studies the interaction between sound and light waves. In imaging we use acousto-optical devices to diffract laser beams through ultrasonic gratings. The acousto-optical effect is based on a periodic change in the refractive index in the high refractive index medium (usually tellurium dioxide, TeO_2) which is the result of the sound wave induced pressure fluctuation in the crystal. This grating diffracts the light beam just like a normal optical grating, but can be adjusted rapidly.

2.1 Acousto-optical Deflection

Acousto-optical deflectors (AODs) control the optical beam spatially, using ultrasonic waves to diffract the laser beam depending on the acoustic frequency. If we introduce a sine wave at the piezoelectric driver, it will generate an optical deflection in the acousto-optic medium according to the following equation:

$$\Delta\Theta_{\mathrm{d}} = \frac{\lambda}{\nu}\Delta f$$

where λ is the wavelength of the optical beam, ν is the velocity of the acoustic wave, and Δf is the change in the sound frequency (Fig. 1).

In practice, AODs or acousto-optical modulators (AOMs) are used. AOMs modulate only the amplitude of the sound waves, while AODs are able to adjust both the amplitude and frequency.

2.2 Acousto-optical Focusing

Besides deflection, AODs can also be used for fast focal plane shifting [33–36]. If the optical aperture is filled with acoustic waves, the frequency of which increases as a function of time (chirped wave), different portions of the optical beam are deflected in different directions (Fig. 2). Thus a focusing, or alternatively a defocusing, effect occurs, depending on the frequency slope (sweep rate) of the chirped acoustic wave. The focal length of an acousto-optical lens (F) can be calculated from the sweep rate as [34]:

$$F = \frac{\nu^2 T_{\mathrm{scan}}}{2\lambda\Delta f}$$

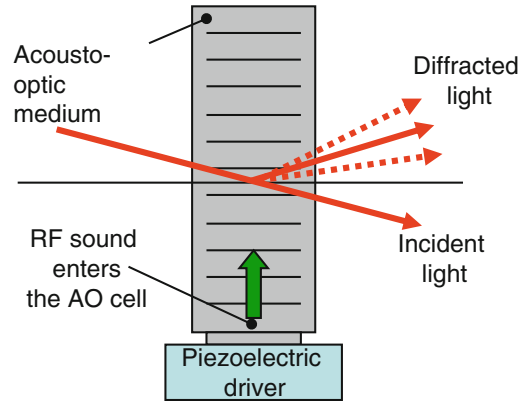

Fig. 1 Operating principle of acousto-optical deflectors. A piezoelectric driver elicits radiofrequency (RF) sound waves due to the externally applied sinusoidal voltage. Sound enters and traverses through the diffracting (TeO_2) medium while interacting with light throughout the aperture. Light is diffracted on the sound wave's refraction index changes as on a steady optical grating providing diffracted light beams whose angle is dependent on the sound wave's frequency

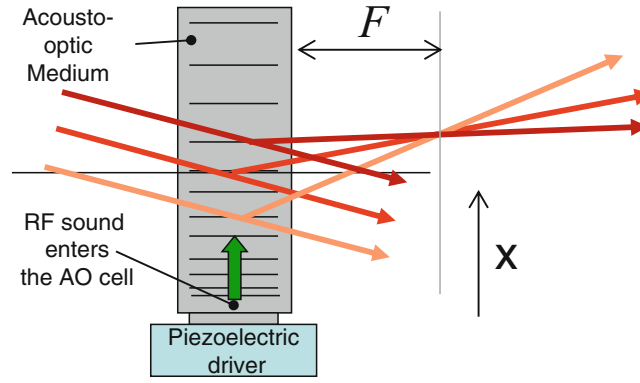

Fig. 2 Acousto-optical focusing. AO deflector arrangement similar to Fig. 1, but here the sound frequency is changing, resulting in a varying grating size along the propagation axis. As a consequence, different parts of the laser beam are diffracted with varying angles creating a focus point whose position can be changed by the parameters of the sound applied to the deflector. *Red* and *orange lines* indicate laser beams and *F* denotes focal distance

where λ is the optical wavelength of the beam, ν is the velocity of the acoustic wave, Δf is the change of the sound frequency, and T_{scan} is the modulation rate of the sound frequency [34].

To keep the focus stable, the frequency gradient should be preserved in the crystal. The frequency should therefore be continuously increased (or decreased) at the piezoelectric driver to preserve the focal distance. This will result in a lateral drift of the focal

point, which can be easily compensated by introducing a second acousto-optical deflector with a counter-propagating acousto-optical wave into the optical pathway [34].

3 3D AO Microscope

3.1 Goals

The ultimate goal in neuroscience is to create a 3D random-access laser scanning two-photon microscope simultaneously satisfying two different needs in the largest possible scanning volume. The first need is to record activity across the dendritic tree of a single neuron in 3D at high spatial and temporal resolution in a central core (approximately $290 \times 290 \times 200\ \mu m^3$) of the scanning volume in a way that dendritic spines remain resolvable. The second need is to record in a more extensive volume (now over $950 \times 950 \times 3000\ \mu m^3$ volume in transparent samples with high NA objectives) at high speed but a relatively reduced resolution, in order to capture all activity from a large number of cell bodies in a neuronal population.

3.2 Selection of the Optimal Concept for Fast 3D Scanning by Optical Modeling

Acousto-optical deflectors and lenses provide fast, programmable tools for addressing regions in 3D. The optical grid generated within the acousto-optical deflector is equivalent to a cylindrical lens. In 3D two-photon microscopy, we need to scan points. Therefore, a combination of two perpendicularly oriented cylindrical lenses with the same focal distance is required. As both acousto-optical lenses (x, y) require drift compensation, 3D microscopes need (at least) four AO deflectors (x1, y1, x2, y2). The four AO deflectors can be optically coupled using *afocal projections* (telescopes with two lenses where the distance between the lenses is equal to the sum of each lens' focal length) and air in different combinations (Fig. 3). There are several possible arrangements of passive optical elements and AODs which can result in a 3D microscope (Fig. 3).

A detailed optical model in ZEMAX (and OSLO) is required to find those combinations of all active and passive optical elements in the scanning light path of the microscope which would provide the maximal exploitation of the apertures of all lenses within the 20× objective (numerical aperture, NA = 0.95) at different x-, y-, and z-scanning positions, and therefore result in the smallest PSF in the largest possible scanning range (Fig. 4). According to the optical models, the largest scanning volume can be reached by grouping the deflectors into two functionally distinct groups (z-focusing and lateral scanning) which are coupled together by one afocal projection (see version #5 in Fig. 3) [33], because this arrangement has several optical advantages. For example, limiting the beam divergence settings at the first group of deflectors allows better transmission, and hence larger scanning volume, because the incident angle tolerance of the AODs in the second group is limited.

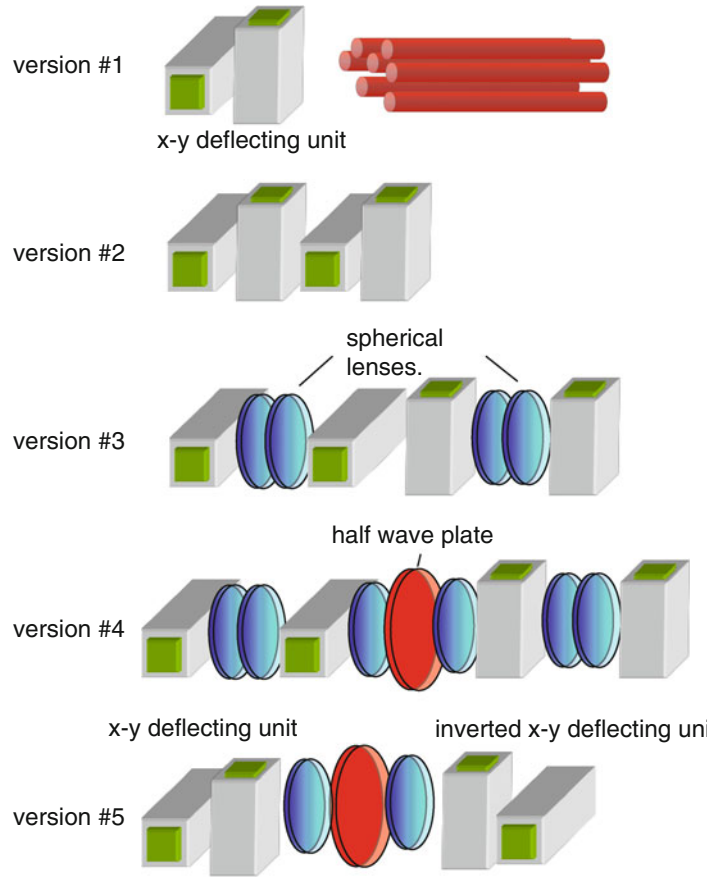

Fig. 3 Different arrangements for 3D AO scanning. Version #1: This was the first realization of a 3D microscope (Rozsa et al., 2003, ISBN 963 372 629 8). The concept uses optical fibers to position the excitation beam in 3D [32]. However, complex mechanical devices are required for each scanning point, which made implementation difficult. Version #2 [35, 37] and version #4 [36, 38–40] have also been described by other laboratories and have recently been used for functional measurements [35, 36]. Versions #2–5 were analyzed by modeling and version #5 was found to be the best [33]. For example, version #5 can provide around two order of magnitude larger scanning volume than other versions

3.3 New Concept for Angular Dispersion Compensation

As AODs are diffractive elements, it is crucial to have a proper compensation for angular dispersion. Angular dispersion is traditionally compensated with prisms [41]. However, 3D scanning requires spatially variable dispersion compensation. The angular dispersion is inherently compensated for following the last (the fourth) AOD in the main optical axis (Fig. 5). However, if we move away from the main optical axis we can find that dispersion increases as a function of distance (Fig. 5). Prisms with increasing apex angle would be required in order to compensate for this

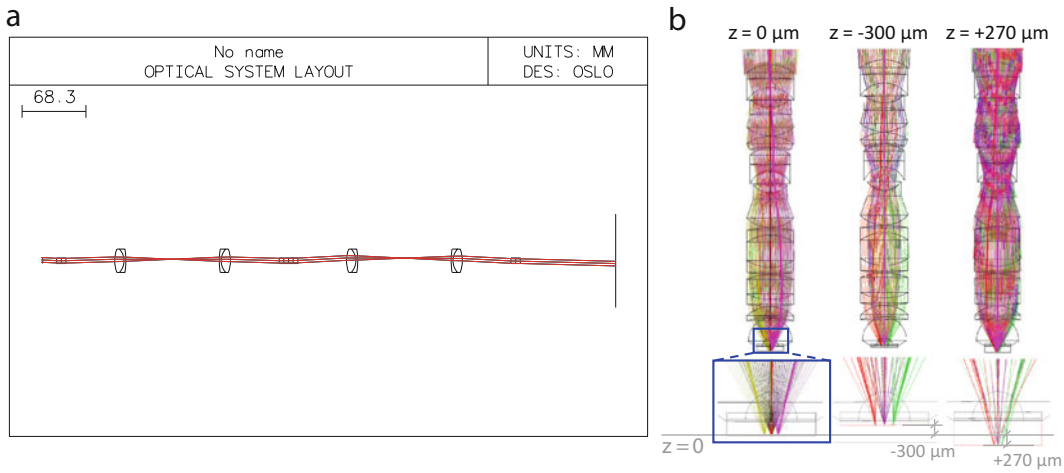

Fig. 4 Optical modeling. (**a**) Print screen showing an optical layout of the 3D microscope's scan head (version #5). (**b**) One of the main optimization criteria during modeling was to fill all the lenses of the objective at variable scanning positions in order to keep the high NA, hence the good PSF, during 3D scanning in the largest volume

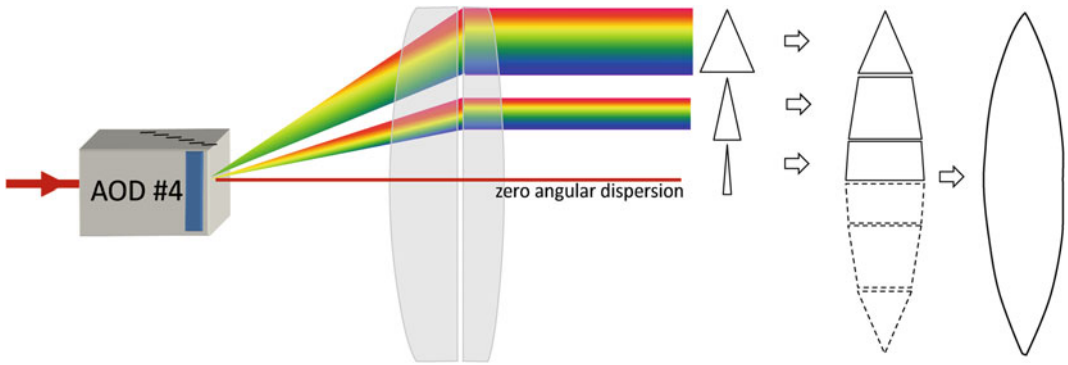

Fig. 5 Concept of angular dispersion compensation

dispersion. However, due to the limited space this theoretical solution does not work. If we make these small prisms wider and "connect" them (in theory, *see* Fig. 5) we can generate a surface which looks like a lens (Fig. 5).

In order to calculate the surface equation of this lens element, we need to go back to the general equation of prisms. The amount of angular dispersion which one prism can compensate for can be matched by properly selecting the incidence angle α_1 and the prism's opening angle α_P. The output angle (α_2) after the prism is given by:

$$\alpha_2(\alpha_1, \alpha_P, \lambda) = a\sin\left(n(\lambda)\sin\left(\alpha_P - a\sin\left(\frac{\sin(\alpha_1(\lambda))}{n(\lambda)}\right)\right)\right),$$

where $n(\lambda)$ is the refractive index. The wavelength-dependent incidence angle can be determined from the rotation angle of the prism β relative to the optical axis, hence the wavelength-dependent angle of propagation of the diffracted beams θ_{def}:

$$\alpha_1(\lambda) = \theta_{def}(\lambda, f_1, f_2) - \beta,$$

and the total deflection angle of the prism:

$$\Delta\alpha(\alpha_1, \alpha_P, \lambda, f_1, f_2) = \theta_{def}(\lambda, f_1, f_2) + \beta - a\sin\left(n(\lambda)\sin\left(\alpha_P - a\sin\left(\frac{\sin(\theta_{def}(\lambda, f_1, f_2) - \beta)}{n(\lambda)}\right)\right)\right) - \alpha_P,$$

The zero angular dispersion requirement after the prism can be expressed as:

$$\frac{\partial[\Delta\alpha(\alpha_1, \alpha_P, \lambda, f_1, f_2)]}{\partial\lambda} = 0$$

The beams deflected at different frequencies in the scanner are spatially separated in the focal plane of the first part of this unit. The different optical wavelength components in each deflected wave are also spatially and angularly dispersed in this plane, and their dispersion also increases as the deflection angle increases, but their spatial dispersion is an order of magnitude less than the separation caused by the acousto-optic deflection. In this case, the angular dispersion increases symmetrically with the distance from this axis, r ($r = \sqrt{x^2 + y^2}$).

The optimal surfaces, however, are not spherical surfaces, but can be expressed as aspheric and conic surfaces with the primary radii given by the equations:

$$c = \frac{\frac{1}{R_1}r^2}{1 + \sqrt{1 - (1 + k_1)\frac{r^2}{R_1}}} + \sum_{n=1:6} a_n r^n$$

where the k_1 conic and a_n aspheric parameters are determined by optical modeling. The value of the radius and the minimum glass thickness at the optic axis is also determined with optimization using the ZEMAX optimization algorithms. Two merit functions are consecutively used, one containing the angular dispersion and aperture in front of the objective, and a second targeting the minimum spot size in the sample plane (the focal plane of the objective). Iteration of these two leads to optimized lens surfaces for the given material and the problem set (see details in Katona et al. [33]).

When comparing a 3D setup using a simple telescope instead of a telescope with the lens element described above, we can obtain a lateral field of view which is ~2-fold larger, with the same focused spot size and dispersion at the edges of this area (*see* Fig. 8 below).

3.4 Construction of the Optical Pathway of a 3D Microscope

According to the optimal arrangement suggested by the optical model [33], a large-aperture (15–17 mm) optical assembly is needed (Fig. 6). A Ti:sapphire laser with automated dispersion compensation provides the laser pulses. The optimal wavelength range is 740–890 nm (but can now be extended to over 1064 nm). A *Faraday isolator* blocks the coherent backreflections (BB8-5I, Electro-Optics Technology). On top of the adjustable pre-chirping provided by the laser source, a fixed four-prism sequence [42] adds a large negative second- and third-order dispersion ($-72{,}000$ fs^2 and $-40{,}000$ fs^3) in order to pre-compensate for pulse broadening caused by the optical elements in the system (*Proctor and Wise* dispersion compensation unit, Fig. 6) [42]. An automated *beam stabilization unit* (see below) is necessary to precisely stabilize the laser beam in the long optical pathway, and cancel out subtle thermal drift errors. The beam stabilization unit is built from position sensors (*q*, quadrant detectors, PDQ80A, Thorlabs), two backside custom-polished broadband mirrors (BB2-E03; Thorlabs), and motorized mirrors (AG-M100N, Newport), wired in a feedback loop. The positioning feedback loop (U12, LabJack Corporation) is controlled by a program written in LabView (National Instruments). The beam is then magnified by a *beam expander* consisting of two achromatic lenses arranged in a Galilean telescope ($f = -75$ mm, ACN254-075-B, Thorlabs; $f = 200$ mm, NT47319, Edmund Optics; distance = 125.62 mm) to match the large apertures of the first pair of AO deflectors (15 mm). Mirrors, $\lambda/2$ waveplates, and holders were purchased from Thorlabs and Newport. AO deflectors have been custom designed and manufactured at the Budapest University of Technology and Economics. These deflectors form two orthogonal electric cylinder lenses filled with continuously changing frequency ("chirped") acoustic waves [34] and are used for *z*-focusing (*AO z-focusing unit*). Next, laser beams from the *x* and *y* cylindrical lenses are projected to the *x* and *y* AO deflectors (17 mm apertures) of the *2D-AO scanning unit*, respectively, by telecentric projection. Achromatic telecentric relay lenses were purchased from Edmund Optics ($f_{TC} = 150$ mm, NT32-886). The *2D-AO scanning unit* performs lateral scanning and also compensates for the lateral drift of the focal point generated by the cylindrical lenses during *z*-focusing [34] (*drift compensation*). *The angular dispersion compensation unit* optically links the 2D-AO scanning unit and the objective. This unit consists of two achromatic lens doublets, and one aspheric and conic lens element for angular dispersion

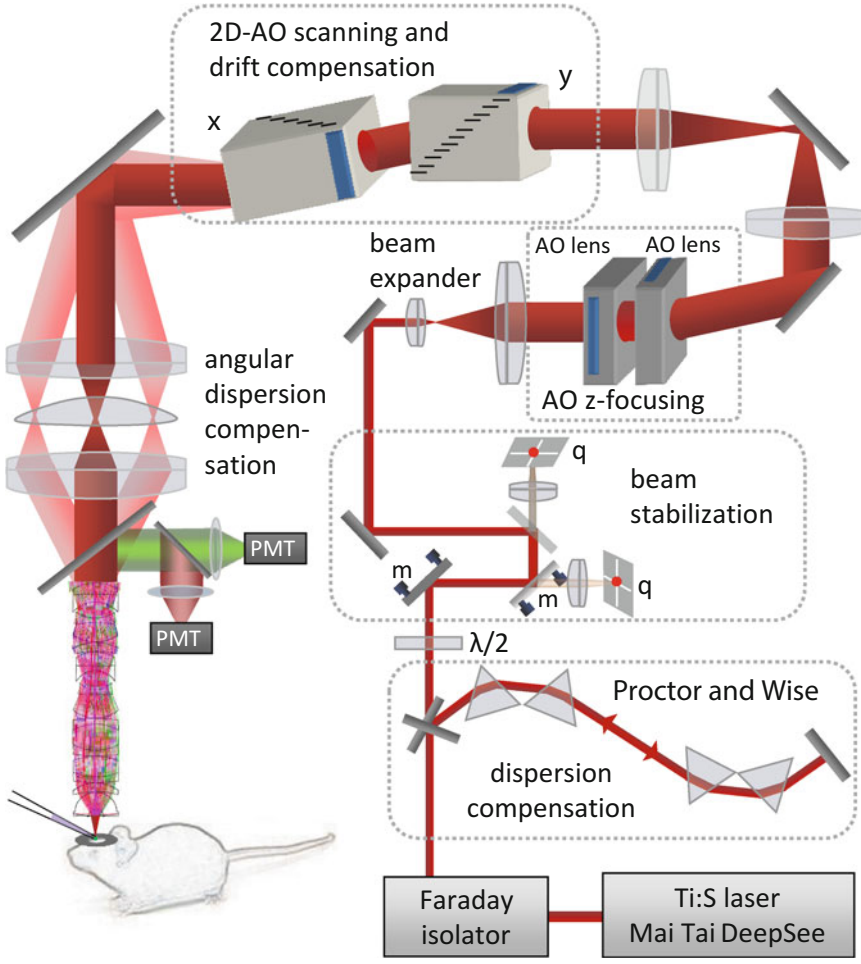

Fig. 6 Design and characterization of the two-photon microscope setup. (**a**) Schematics of the microscope setup. Material-dispersion compensation is adjusted with a four-prism compressor (Proctor and Wise) and a Ti:sapphire laser. A Faraday isolator eliminates coherent backreflections. Motorized mirrors (*m*) stabilize the position of the beam light on the surface of two quadrant detectors (*q*) before the beam expander. Two AO deflectors optimized for diffraction efficiency control the *z*-focusing of the beam (AO *z*-focusing). A two-dimensional AO scanner unit (2D-AO scanning) performs *x*–*y* scanning and drift compensation during *z*-scanning. A spherical field lens in the second telecentric lens system ($Tc_{3,4}$) provides additional angular dispersion compensation

compensation (Fig. 6). Achromatic scan and tube lenses were chosen from Edmund Optics ($f = 250$ mm, NT45-180) and Olympus ($f = 210$ mm), respectively. Finally, the AO-based 3D scanner system is attached to the top of a galvanometer-based upright two-photon microscope (Femto2D-Alba, Femtonics Ltd.) using custom-designed rails. AO sweeps are generated by the direct digital synthesizer chips (AD9910, 1 GSPS, 14-bit, Analog Devices) integrated into the modular electronics system of the microscope using FPGA elements (Xilinx). Red and green fluorescence are separated by a dichroic filter (39 mm, 700dcxru, Chroma

Technology) and are collected by GaAsP photomultiplier tubes custom-modified to efficiently collect scattered photons (*PMT*, H7422P-40-MOD, Hamamatsu), fixed directly onto the objective arm (Travelling Detector System). In in vitro experiments the forward-emitted fluorescence can also be collected by 2-in. aperture detectors positioned below the condenser lens (Femto2D-Alba, Femtonics). Signals of the same wavelength measured at the epi- and transfluorescent positions are added. The large aperture objectives, XLUMPlanFI20×/0.95 (Olympus, 20×, NA = 0.95) and CFI75 LWD 16XW (Nikon, 16×, NA = 0.8), provide the largest scanning volume (Katona et al. [33]). The maximal output laser power in front of the objective is around 400 mW (at 875 nm).

3.5 Controlling 3D AO Scanning

3.5.1 Generating Driver Signals for 3D AO Scanning

To focus the excitation beam to a given x,y,z-coordinate, the four AODs should be driven synchronously with varying frequency voltage signals. Because AODs have limited electrical bandwidths, changing frequency can be maintained only for a limited time, before the frequency has to be abruptly reset. This sudden transient in the driving frequencies results in an improperly formed focal point and can therefore be considered as "dead time" (Fig. 7). The length of this period is defined by the time taken by the acoustic wave to travel through the optical aperture of the crystal (usually in around 5–30 μs).

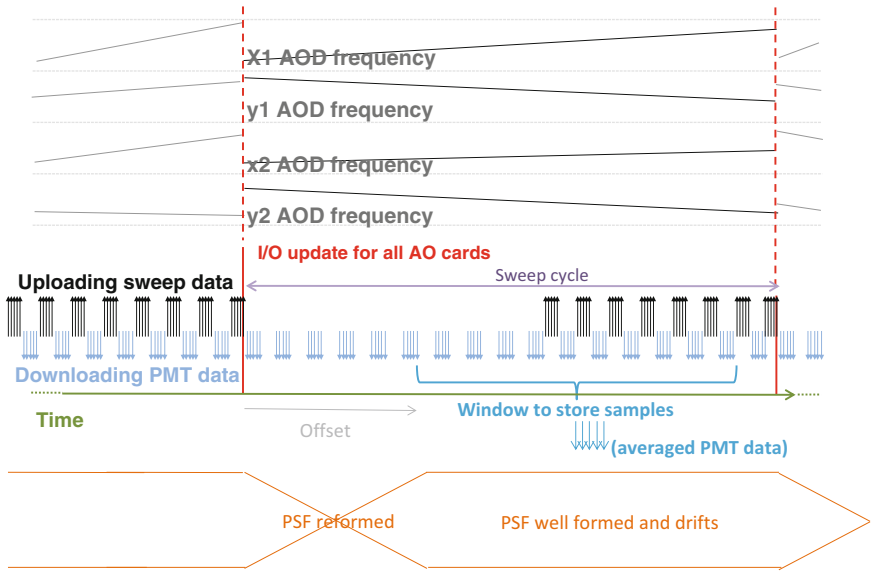

Fig. 7 Driving functions and operation of the four-detector sequence. (*Top*) The four upper traces show the frequency modulation of the sine wave as a function of time at the four acousto-optical deflectors (x1, y1, x2, y2) within one and a half sweep cycle. (*Middle*) PMT data are continuously collected and transferred to the computer. PMT data collected during the "offset" period are eliminated in the analysis process. *Red lines* show the synchronous frequency reset of the driver functions

The position and the movement of the focal point are determined by eight values. Four of them control the starting acoustic frequency of the four AOD drivers, while the other four define the frequency ramp speeds (chirping). All of the eight parameters are updated in every sweep cycle (typical cycle time is 33.6 μs). The starting frequencies and the chirps together define the *xyz* position of the focal spot and its *xy* movement speed (drifting). During every sweep cycle all PMT channels are sampled multiple times. The ratio of the dead time (offset time) and the measurement time (when the focal point has already been formed and is ready for imaging) depends on the *z*-level and is optimal at the nominal focal plane of the objective.

In the simplest case, the goal is to attain a steady focal point with no lateral drifting (random-access scanning mode). In this scanning mode, PMT data are averaged and one value is created for each measurement cycle, corresponding to a single point in *x*,*y*, *z*. Thus, this mode allows random-access 3D point scanning which is ideal for monitoring neuronal network activity. More complex measurement modes are possible when the focal point is allowed to drift, such as during Multiple 3D Trajectory Scanning.

We can also take advantage of the active optical elements to dynamically compensate for optical errors (astigmatism, field curvature, angular dispersion, chromatic aberration) by changing the AOD control parameters: this increases spatial resolution, especially during AO *z*-focusing (at $z \neq 0$ planes by a factor of ~2–3; see "no electric compensation" in Fig. 8).

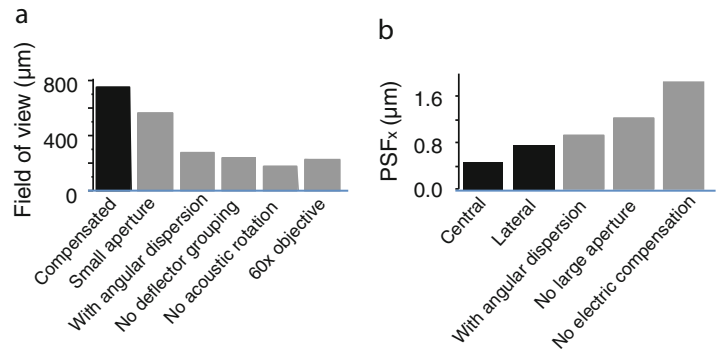

Fig. 8 Characterization of the two-photon microscope setup. (**a**) The maximal field of view (compensated) is shown when both deflector pairs were used for deflection (no deflector grouping) or when optically rotated deflectors (no acoustic rotation), small aperture objectives (60×), no angular dispersion compensation (with angular dispersion), or small aperture acousto-optic deflectors were used (small aperture). (**b**) The compensated PSF size along the *x*-axis (PSF_x) (central) at (x, y, z) = (150, 150, 100) μm coordinates (lateral) or when no angular dispersion compensation (with angular dispersion), no electronic compensation (no electric compensation) or reduced AO apertures were applied (no large apertures)

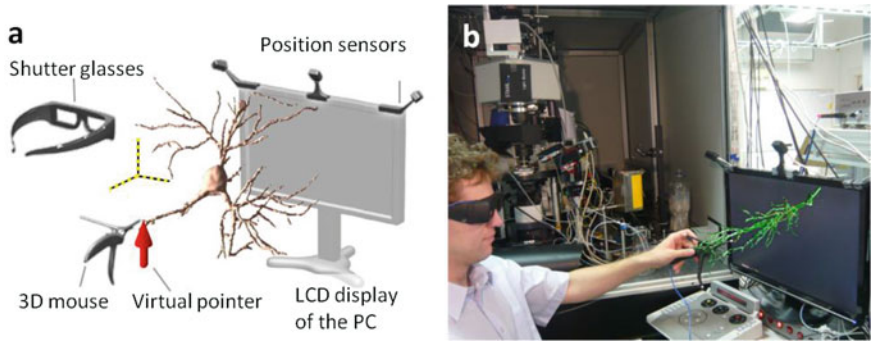

Fig. 9 3D virtual reality environment for 3D two-photon imaging. (**a**) Using the 3D virtual reality environment, the 3D measurement locations can be freely modified or observed from any angle. Head-tracked shutter glasses ensure that the virtual objects maintain a stable, "fixed" virtual position even when viewed from different viewpoints and angles, i.e., the cell's virtual coordinate system is locked in space when the viewer's head position (view angle) changes; however, it can be rotated or shifted by the 3D "bird" mouse. The bird also allows the 3D measurement points to be picked and repositioned in the virtual 3D space of the cell. See also Materials and methods. (**b**) Image of the 3D AO setup and the experimenter using the 3D virtual reality environment (Katona et al. 2012)

The optimal compensation parameters need to be determined in advance for each point of the scanning volume, and loaded into the driver electronics accordingly. During this optimization process the parameters of the chirped sine driver function need to be varied at each of the four deflectors in order to maximize the fluorescence intensity and the sharpness of the fluorescent beads used during this calibration process.

3.5.2 User Interface

Standard user interface modules (GUIs) can also be used for controlling 3D microscopes. In the simplest realization, the optimal "z" coordinate is selected first, then using a PC mouse we can easily pick up the x and y coordinates from the background images, which were taken in advance and are shown according to the selected z coordinate.

Thanks to rapid developments in the field of 3D video, we can now implement more sophisticated solutions for controlling 3D measurements. For example, the use of a 3D pointer in combination with a 3D video projector and a head position sensor in a 3D virtual reality environment allows points (or guiding points which determine a 3D object) to be selected for 3D acousto-optical scanning (Fig. 9).

3.6 Advantages of the Detailed Optical Design

One difference between the system described here and previous designs is that the AO deflectors form functionally and physically different groups. The first AO pair is used for z-focusing, whereas lateral scanning is performed entirely by the second pair (*2D AO scanning unit*). This arrangement increases the diameter of the lateral scanning range by a factor of about 2.7 (Fig. 8).

Furthermore, not only electronic driver function but also deflector geometry, TeO_2 crystal orientation, and bandwidth are different between deflectors of the *z*-focusing and the 2D AO scanning units. Altogether, these factors increase the diameter of the lateral scanning range to 720 μm using the Olympus 20× objective, and to over 1100 μm when the Nikon 16× objective is used (Fig. 8). Spatial resolution in the whole scanning volume is also increased by the large optical apertures used throughout the system, and about 20 % of this increase is due solely to the use of large AOD apertures (Fig. 8). In contrast to the dominantly *z*-focusing-dependent effect of dynamic error compensation, the angular dispersion compensation unit decreases the PSF in off-axis positions when compared with a simple two-lens telecentric projection (Fig. 8b). These factors which decrease the PSF inherently increase the lateral field of view (Fig. 8a).

3.7 Scanning Modes

Multiple scanning modes have been developed for AO scanning; these can also be used in different combinations as needed by the experimental protocols.

3.7.1 Random-Access Point Scanning

Random-access scanning is one of the most convenient applications for imaging neuronal networks in 3D. In the first step, a reference *z*-stack image is acquired (see later Figs. 19, 20, 21, and 22). In the second step, points can be preselected for fast 3D measurements. Once a region with well-stained cells has been identified, one or more reference structures (typically a brightly red-fluorescing glial cell) can be selected, scanned in 3D, and the 3D origin [(0, 0, 0) coordinate] of the recording defined as the center of this glial cell. In order to compensate for tissue drift, the "origin-glia" cell must be re-scanned regularly during an experiment and moved back into the original position (0,0,0) by moving the microscope table and the objective. Three-dimensional Ca^{2+} responses recorded simultaneously at multiple points can be plotted as curves or, alternatively, responses following spatial normalization can be shown as images (see later Figs. 19, 20, 21, and 22).

3.7.2 Frame Scanning in 3D

One of the basic measurement modes which can be realized with a 3D AO microscope is frame scanning. In this mode one can freely move or rotate arbitrary areas in 3D using the real *z* (by moving the objective) and virtual *z* (by focusing with the AO deflectors at a fixed objective position) for focusing. Since the 3D Frame Scanning mode is relatively slow, this mode can be used to find and preselect ROIs for subsequent fast 3D measurements. Alternatively, multiple areas situated in multiple layers can be selected and measured simultaneously. For example, we can simultaneously measure the basal and apical dendritic regions of pyramidal cells, or image layer II/III and layer V cells simultaneously.

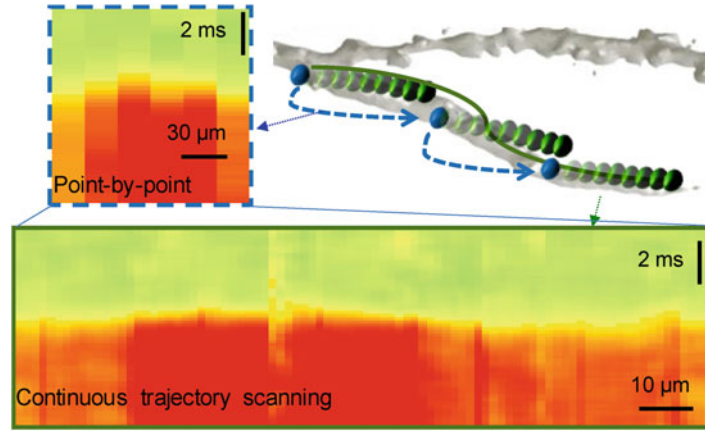

Fig. 10 Comparison of point-by-point and continuous 3D trajectory scanning modes. *Top right*, schema of the scanning modes (*blue*, point-by-point scanning; *green*, continuous scanning). Example of Ca^{2+} responses measured by point-by-point (*top left*) and continuous trajectory scanning modes (*bottom*). Ca^{2+} responses were spatially normalized

3.7.3 Multiple 3D Trajectory Scanning

This mode was developed for simultaneous measurement of multiple neuronal processes. There are two realizations of 3D trajectory scanning. In the Continuous Trajectory Scanning mode, instead of jumping between preselected points (as during by point scanning), the focal point is allowed to drift along neuronal processes (Fig. 10). Information is therefore collected with a much higher spatial discretization within the same time interval.

3.7.4 Volume Imaging

It is possible to capture volumetric data by successively capturing *xy* images at different *z* positions. The jump between the *z*-planes can be obtained by using either the real or the virtual focus. The first will result in better optical quality; therefore it can be used at the end of experiments if only the volume information is required. However, if fast 3D line scanning, 3D frame scanning, or random-access scanning is required, the *z*-stack should be obtained using virtual focusing in order to precisely preserve the coordinates of the cells for the fast 3D AO scanning because the coordinate system of 3D AO microscopes is distorted. Alternatively, a coordinate transformation is needed to correlate the information in the two *z*-stacks.

3.8 Characterizing the Optical Performance of the 3D Microscope

To test the performance of our microscope, the 3D location of fluorescent beads must be imaged to confirm that the microscope can focus and stabilize the PSF at different depths. For example, the stability of fluorescence signals can be measured by repetitively AO-scanning preselected points only, using a short (1.6–16.8 µs) pixel dwell time and a short, 10–20 µs positioning time (typically 16.8 µs, the positioning time is determined by the diameter of the

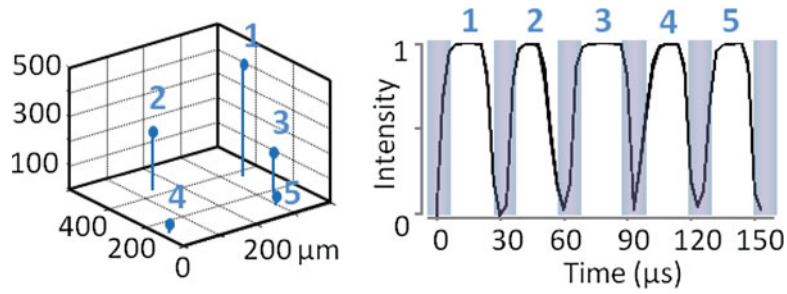

Fig. 11 Stability of 3D AO scanning in random-access mode. (*Left*) Location of the five fluorescent beads (diameter, 6 µm) repetitively scanned in a 3D sample. (*Right*) Five overlaid fluorescence measurements showing dead times (*gray*) and windows of properly formed and positioned PSF (*white*)

optical beam in AODs). These time parameters result in a measurement speed in a range from about $23.8/N$ kHz to $54.3/N$ kHz (where N denotes the number of points, typically ranging from 2 to 2000; Fig. 11).

Then the PSF size must be determined at different points in the accessible volume (Fig. 12). The full-width-at-half maximum (FWHM) values of the PSF in the center of the objective are typically slightly larger (for the Olympus 20×, 470 nm, 490 nm, and 2490 nm along the x, y, and z axes, respectively, Fig. 12a) than those compared to the ones measured with a two-dimensional microscope, where the optical pathway is typically more simple.

Although spatial resolution decreases with radial and axial distances from the center of the objective focus (Fig. 12b, c), PSF size remains small (diameter < 0.8 µm, axial length < 3 µm) in the central core of the volume (~$290 \times 290 \times 200$ µm^3), allowing the resolution of fine neuronal processes. Moreover, PSF size, being below 1.9 µm diameter and 7.9 µm axial length in an approximately 1400 µm z and 700 µm lateral scanning range, allows the optical resolution of individual fluorescent beads whose radius, 6 µm, is smaller than the average diameter of neuronal somata (Fig. 13).

With the help of the AO driver electronics featuring dynamic compensation, the diffraction efficiency inhomogeneities of the AO deflectors and also, partially, the drop of intensity at the sides of the images can be compensate for (Fig. 14).

One of the main advantages of 3D scanning over other 3D technologies is that the wide bandwidth of the AO deflectors allows precise targeting of the center of the focal point (with 51 nm and 140 nm accuracy in the whole volume along radial and axial axes, respectively, which is around 10 % of the optimal PSF size for the system proposed in Fig. 6). Therefore, PSF can be precisely localized in the middle of neurons, avoiding neuropil contamination.

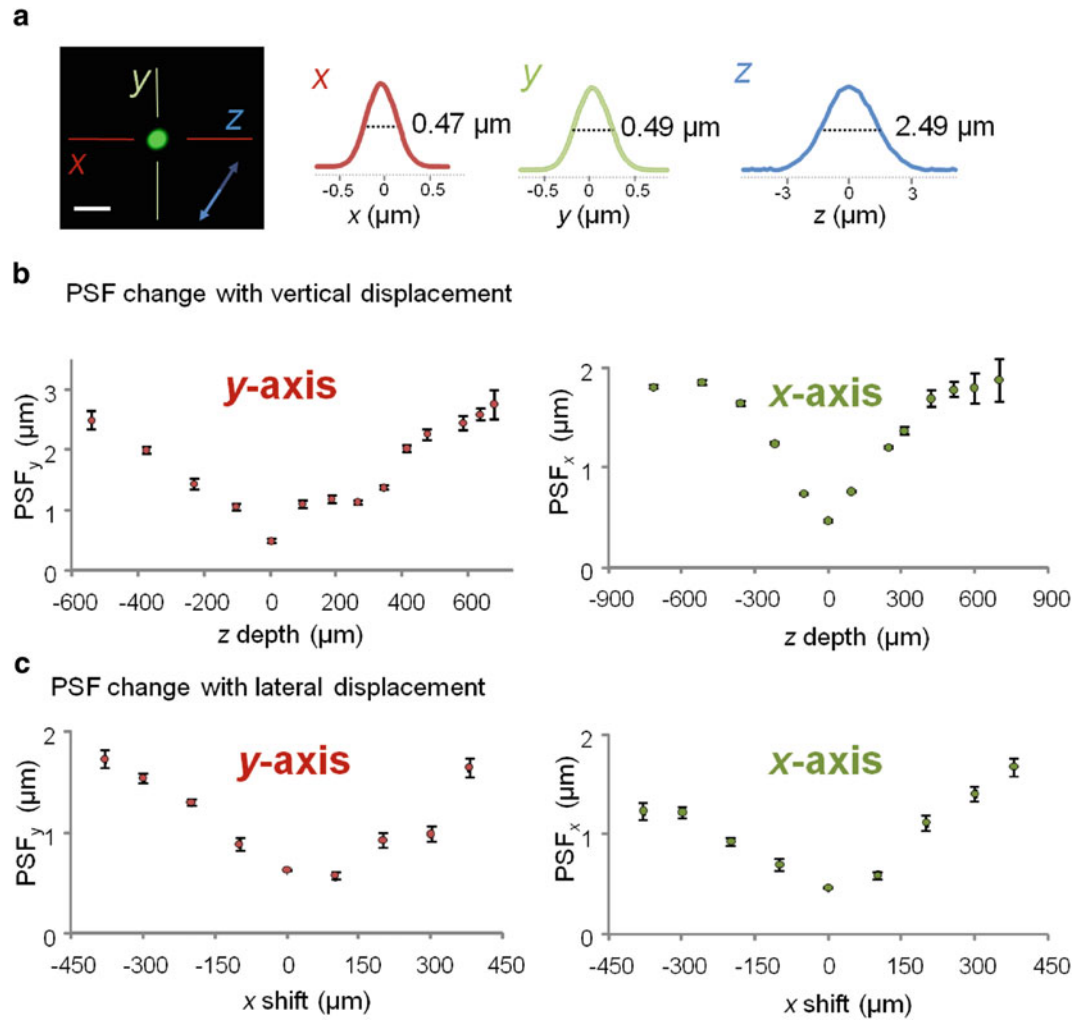

Fig. 12 Size of the PSF in the 3D AO scanning volume. (**a**) A fluorescent bead (0.1 µm) imaged with the optically optimized system utilizing electronic optimization using the 20× objective in the center (x, y, z) = (0, 0, 0) µm coordinates. Corresponding intensity profiles along (x, y, z) axes with full-width-at-half maximum (FWHM) values. Note radial symmetry in center. Scale bar, 1 µm. (**b**) Measured PSF diameters along the x and y axes are plotted as a function of axial AO z-scanning displacement from the nominal object plane of the objective (nominal object plane is also known as front focal plane). (**c**) PSF diameters along the x and y axes are plotted as a function of lateral displacement from the center of the nominal object. The 20× objective (Olympus XLUMPlanFI20×/0.95) was used for these two-photon measurements whose parameters were also implemented in optical modeling

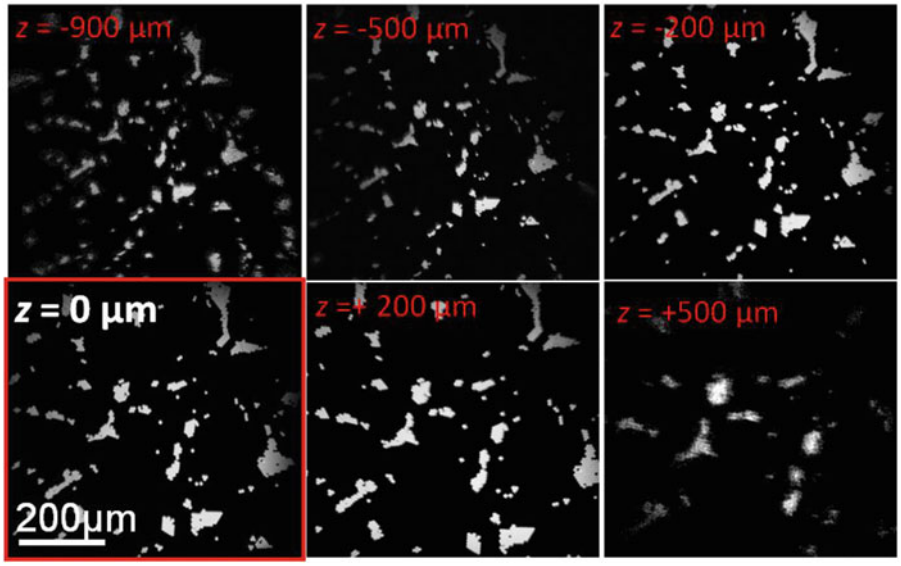

Fig. 13 Fields of view of the 3D microscope system. The analyzed sample consisted of 6-µm-diameter fluorescent beads on a cover glass. AO *z*-focusing was compensated for by refocusing the objective mechanically to keep the fixed sample in focus. The inscriptions show objective shifts along the *z*-axis required for refocusing. The maximal field of view of the system was approximately 700 µm at $z = 0$ µm. $z = 0$ was defined as the nominal object plane. Importantly, lateral displacement of the field of view and change in magnification as a function of AO *z*-focusing need to be compensated for in the acquisition program. Individual beads remained visible in a 1400 µm scanning range

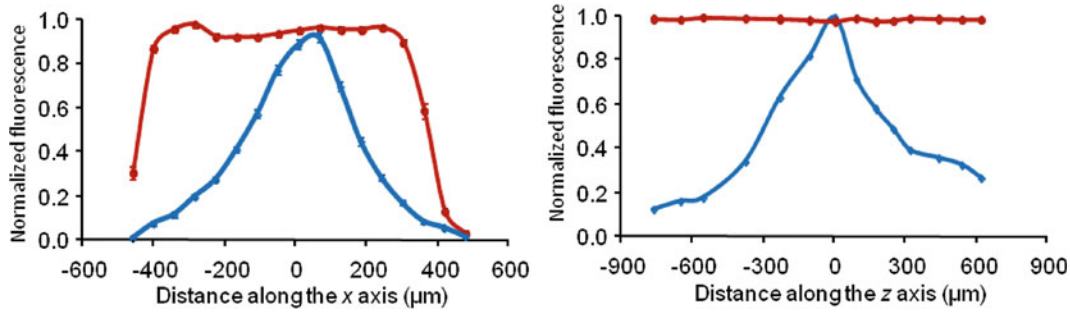

Fig. 14 Maximal FOV of the microscope system with dynamic compensation. Normalized fluorescence intensity as a function of distance from the origin along the *x* and *z* axes with (*red*) and without (*blue*) dynamic compensation. Measurements were performed in a homogeneous fluorescence sample. The fluorescence intensity is affected by the variations in both the excitation intensity and the PSF size (*blue*). In contrast to previous experiments, these technical shortcomings in the driving signals were compensated for by varying both their frequency and power in advance using the dynamic compensation software module (*red*) (from Katona et al. 2012)

In order to properly validate the 3D microscope, the parameters need to be tested in a biological context.

4 In Vitro and In Vivo Testing of the 3D AO Microscope

4.1 3D Random-Access Scanning of Action Potential Propagation

To examine the temporal resolution of a 3D system, imaging one of the fastest regenerative events is the optimal choice. In order to achieve this goal, we can for example measure backpropagating action potentials at multiple 3D locations in a single hippocampal neuron in acute hippocampal mouse brain slices (Fig. 15). Neurons, for example CA1 pyramidal cells, need to be patch-clamped in whole-cell mode and filled with the green fluorescent Ca^{2+} sensor Fluo-5F and the red fluorescent marker Alexa594. The objective must be positioned at the correct depth, such that the center of the region of interest is in focus. The objective is fixed at this position and a reference *z*-stack of images is acquired using 3D AO scanning

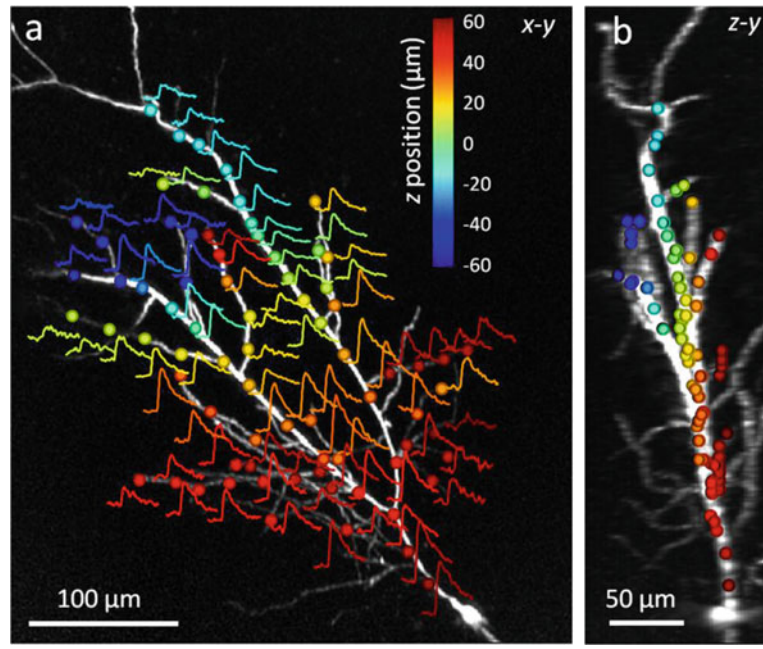

Fig. 15 Three-dimensional measurement of bAPs. (**a**) Maximum intensity *z*-projection of the dendritic arbor of a CA1 pyramidal cell imaged by 3D AO scanning. *Circles* represent the 77 preselected measurement locations for 3D random-access point scanning. *Overlaid curves* show Ca^{2+} transients recorded near-simultaneously in each location, induced by a single bAP (each is the average of five traces). The repetition rate of the measurement was 29.76 kHz (0.39 kHz speed in each location). The *z*-coordinates of the measurement locations are color coded. (**b**) Maximum intensity side projection of the cell with the measurement locations shown in (**a**)

only. Points along the dendritic tree of one single neuron can be selected from the *z*-stack using either a 3D virtual environment (Fig. 9, see also Sect. 3.4.2) or by scrolling through the *z*-stack in a 2D virtual environment [2]. When the cell is held in current-clamp mode, APs can be evoked by somatic current injection while near-simultaneously measuring dendritic Ca^{2+} signals associated with the backpropagating action potentials (bAPs) by repetitively scanning the selected 3D coordinates at 29.76 kHz. When sample drift occurs during measurements, the measurement points need to be repositioned.

Since acute brain slices are about 300-µm thick, only a fraction of the total AO *z*-scanning range can be used. To test whether random-access 3D AO scanning can record bAP-induced Ca^{2+} transients we can, it is possible for example, move the objective focal plane mechanically from +562 µm to −546 µm away from the *z*-center, then use AO *z*-focusing to refocus the recorded dendritic tree (Fig. 16a) and test for AP resolution. Independent of the AO

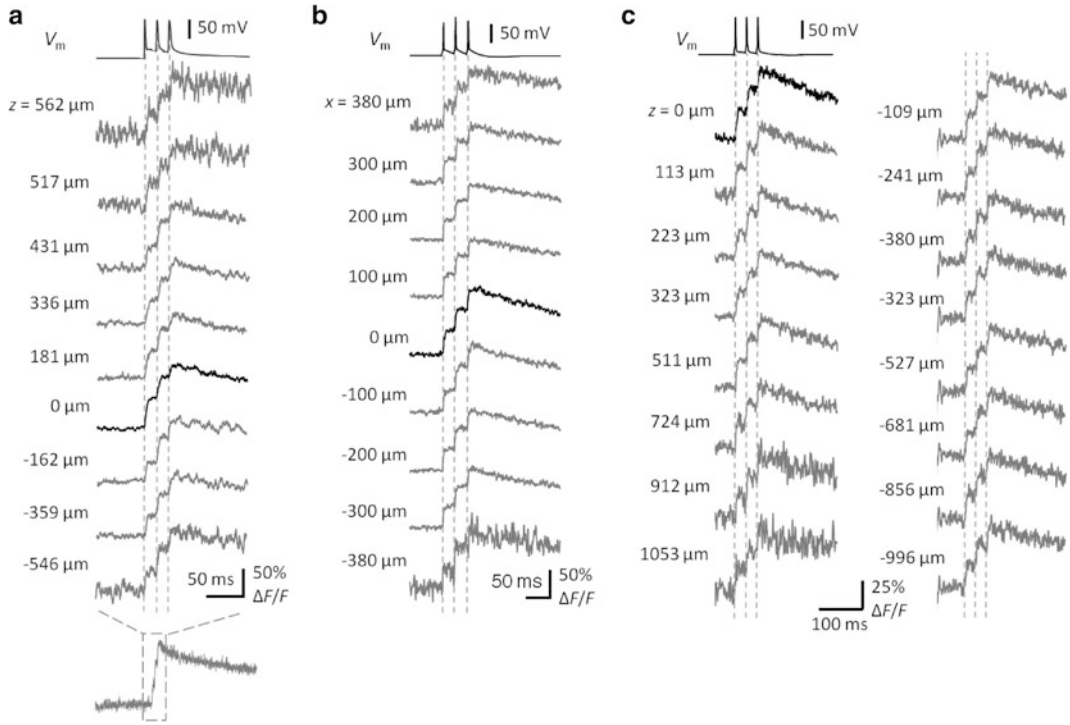

Fig. 16 Resolving bAPs at the sides of the FOV. (**a**) Single traces of three bAP-induced dendritic Ca^{2+} transients measured at the same dendritic point at different AO *z*-focusing settings. To keep the image sharp, the AO *z*-focusing was compensated by mechanical refocusing of the objective. Note the preserved single AP resolution even at the lower and upper limits of the scanning range. Corresponding somatic voltage traces (V_m) are shown on the *top*. (**b**) The same as in (**a**), but transients were recorded while shifting the dendrite along the *x*-axis. (**c**) The same as in (**a**), but single traces were recorded using the 16× Nikon objective. Note that the AO *z*-focusing range with single AP detection level exceeds 2000 µm

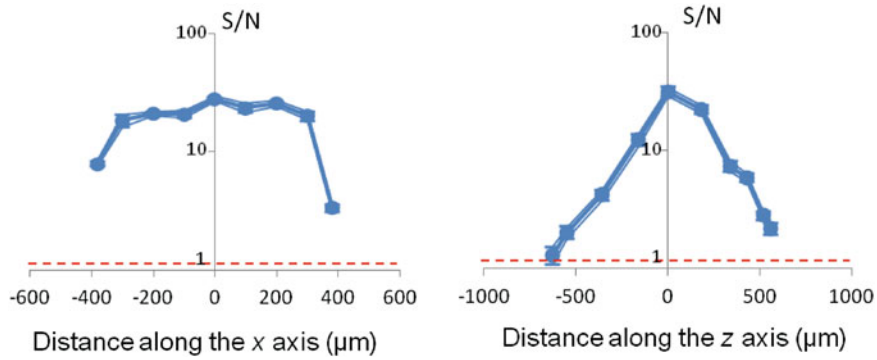

Fig. 17 SNR of bAPs in the field of view. SNR calculated from the pool of transients shown in Fig. 16. Peak of the Gauss-filtered bAP-induced Ca^{2+} transients was divided by the s.d. of the unfiltered 50 ms baseline period (mean ± s.d; $n = 10–50$ transients at each position). Single AP detection level is marked with a *red dashed line*

z-settings, single bAPs could be resolved in Ca^{2+} transients induced by a train of three APs. Similarly, single bAPs could be followed in a large (760 μm) lateral scanning range (Fig. 16b). Thus a total of 1190 μm AO *z*-focusing range and a 760 μm AO lateral scanning range is shown with the 20× objective where single APs can be resolved with signal-to-noise ratio (SNR) greater than 1 (Fig. 17). This range can be extended over 2000 μm with the use of the 16× Nikon objective (Fig. 16c). In summary, resolving single AP-induced transients is possible in a near-cubic-millimeter scanning volume with 3D AO scanning.

The highest temporal resolution of a 3D microscope can be tested by measuring the fast propagation speed of bAPs. Similarly, it is possible to evoke a somatic AP in a pyramidal cell held under current-clamp while scanning in 3D along its dendrite. The bAP-evoked Ca^{2+} transients show increasing latency in dendritic measurements taken further away from the cell body (Fig. 18b). The velocity of the bAP can be calculated from the latency of the Ca^{2+} transients and the distance from the soma (Fig. 18c).

4.2 3D Scanning of Dendritic Spike Propagation

Given the importance of integrating dendritic activity into neuronal information processing [1, 3, 4, 43, 44], the 3D system could also be used to record dendritic spike activity. To measure the extent and spread of local regenerative activity, we can use random-access scanning and detect activity at many discrete points along the 3D trajectory of a dendrite (point-by-point trajectory scanning). As above, we can scroll through a reference *z*-stack of a series of pre-recorded images and select guide points along the length of a dendrite (Sect. 3.4.2). Then, instead of recording from these manually selected points, we can also homogeneously re-sample the trajectory using, for example, piecewise cubic Hermite

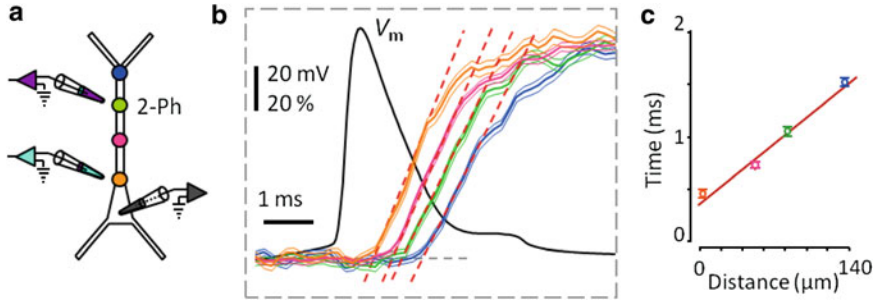

Fig. 18 Measurement of bAP propagation speed. (**a**) Experimental arrangement for signal propagation experiments. Signal propagation speed was measured by simultaneous somatic whole-cell current-clamp (V_m, *black*) and 3D two-photon calcium imaging measurements (*orange*, *pink*, *green*, and *blue*). (**b**) AP peak triggered average of normalized dendritic Ca^{2+} transients induced by APs (mean ± s.e.m.; $n = 54$; *top*). Linear fits (*red dashed lines*) define onset latency times. (**c**) Onset latency times (mean ± s.e.m.; $n = 54$) of Ca^{2+} transients in (**b**) as a function of dendritic distance. Linear fit: average propagation speed. Average bAP propagation speed was 164 ± 13 µm/ms ($n = 9$) at 23 °C

interpolation [2]. This algorithm is better than the conventional spline interpolation because it never overshoots at the guide points. The speed of the 3D measurement depends on the number of recording points along the trajectory.

In the example shown in Fig. 19, a hippocampal CA1 pyramidal cell was filled with Fluo-5F and dendritic Ca^{2+} spikes were induced by focal synaptic stimulation, with an extracellular electrode >400 µm from the cell body. The propagating activity was followed optically at uniformly spaced locations along the main apical dendrite (Fig. 19a). The recorded traces were normalized by calculating $\Delta F/F$ at each point and were projected as a function of time and distance measured along the 3D trajectory line (3D Ca^{2+} responses, Fig. 19b). The Fluo-5F responses revealed dendritic spikes propagating toward the cell body, both when the synaptic stimulation evoked somatic APs (suprathreshold spikes) and when the synaptic stimulation was insufficient to evoke somatic APs (subthreshold spikes, Fig. 19b–e). After a short initiation phase, subthreshold dendritic spikes propagated rapidly and then gradually ceased before reaching the cell body (Fig. 19b). We quantified spike propagation speed by measuring propagation times at the half-maximal amplitude of the transients (Fig. 19c) or at the peak of their first derivatives (Fig. 19d). The average propagation speed was significantly higher for suprathreshold spikes than for subthreshold spikes (subthreshold 81 ± 27 µm/ms, suprathreshold 129 ± 30 µm/ms; 131 %, *t*-test, $P = 0.03$; $n = 7$ cells; Fig. 19e), and both supra- and subthreshold spikes propagated in the direction of the cell body under these conditions (Fig. 19e). Note that, despite the large

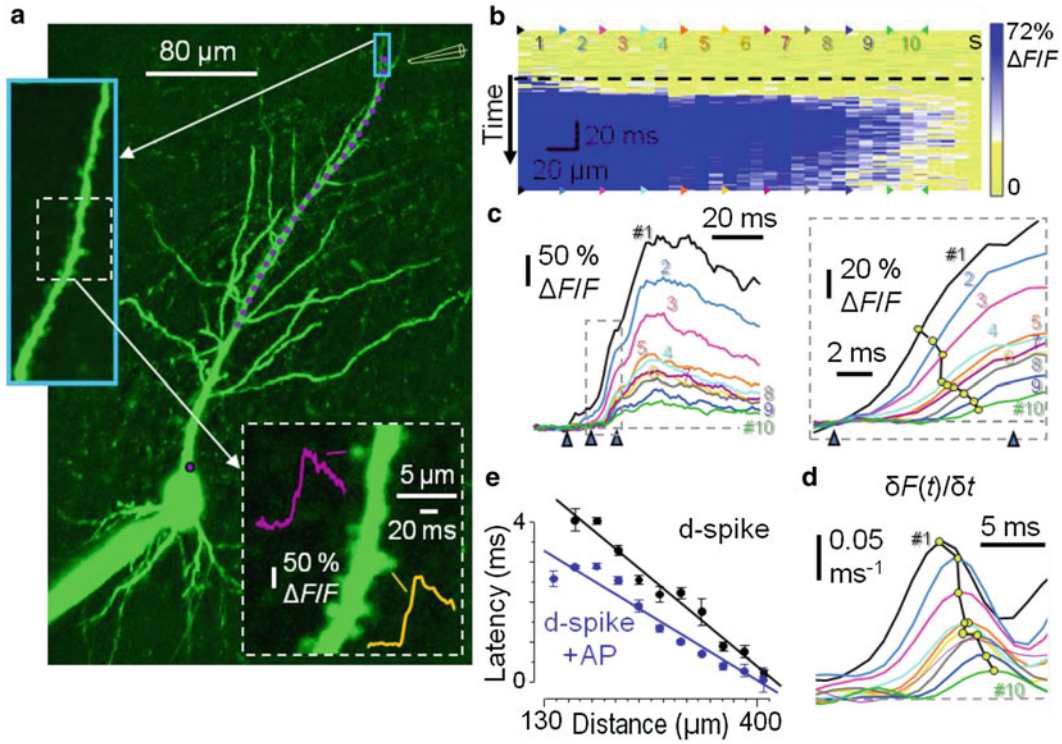

Fig. 19 3D scanning of dendritic Ca^{2+} spike propagation in CA1 pyramidal cells. (**a**) Maximum-intensity projection AO image of a CA1 pyramidal cell. Ca^{2+} transients in dendritic spines (*orange* and *magenta* traces) following induction of dendritic Ca^{2+} spike by focal extracellular stimulation (electrode: *yellow*). *Left* and *bottom insets*, enlarged views. *Purple dots* represent scanning points in a dendrite. (**b**) Spatially normalized and projected Ca^{2+} signals in the dotted dendritic region shown in (**a**) (average of five subthreshold responses). *Black dashed line*, stimulus onset. Column *s*, somatic Ca^{2+} response. (**c**) Ca^{2+} transients derived from the color-coded regions indicated in (**b**). *Right*, Baseline-shifted Ca^{2+} transients measured in the region contained in the *dashed box* in (**a**). *Yellow dots*, onset latency times at the half maximum. (**d**) Onset latency times at the peak of the derivative ($\delta F(t)/\delta t$) of Ca^{2+} transients shown in (**c**). (**e**) Onset latency times as a function of dendritic distance from the soma for somatic subthreshold (*black*) and suprathreshold (*blue*) dendritic Ca^{2+} spikes

total scanning volume (290 × 290 × 200 µm^3), two-photon resolution was preserved (in the range of 0.45–0.75 µm). The total number of measured points along any given trajectory was 23.8–54.3 points per kHz.

4.3 High-Speed In Vivo 3D Imaging of Neuronal Network Activity

To test the performance of the 3D imaging systems in vivo, it is possible, for example, to record Ca^{2+} responses from a population of individual neurons in the visual cortex of adult anesthetized mice. First, we need to inject a mixture of a green Ca^{2+} dye (e.g., OGB-1-AM) to monitor changes in intracellular Ca^{2+} concentrations, and sulforhodamine-101 (SR-101) [45] to selectively label glial cells (Fig. 20). The red fluorescence of SR-101 allows

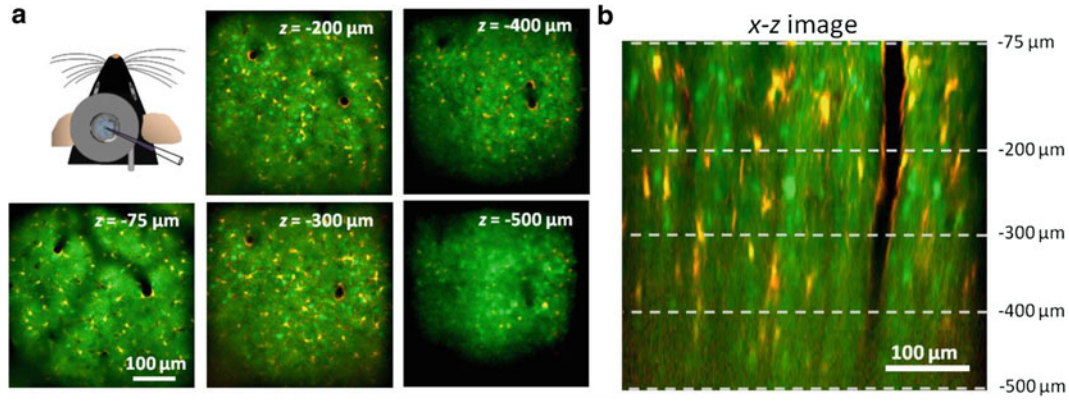

Fig. 20 In vivo image stacks of the neuronal population. (**a**) Representative background-corrected images taken at different depths from the surface of the brain showing neurons (*green*) and glial cells (*red* and *yellow*). *Red* and *green* channel images were overlaid. (*Upper left*) sketch of in vivo experimental arrangement. Staining by bolus loading (OGB-1-AM and SR-101) in mouse V1. (**b**) *x–z* slice taken from the middle of the stack volume *dotted lines* corresponds to the planes in (**a**)

differentiation between neurons and glial cells (green and red, respectively). The maximal power of a Ti:sapphire laser (which is in the range of 3.5–4.5 W) limits the depth of the in vivo recording to a maximum of 500–700 µm from the surface of the cortex (the total imaging volume was about $400 \times 400 \times 500$ µm^3 in Katona et al. [33], and now it is about $600\times 600\times 650$ µm^3 thanks to the ~4-fold increase in transmission efficiency resulting from better AODs).

In the next step, a reference *z*-stack must be recorded. An automated algorithm can identify the neuron and glial cell bodies. When OGB1-AM and SR-101 dyes are bolus-loaded into the animal, cells can be categorized according to their dye content, measured by fluorescence. Neuronal cells can be detected because of their elevated green fluorescence and decreased red fluorescence. The green and red fluorescent channel data of each image can also be normalized in the *z*-stack and then scaled and shifted so that the tenth and 90th percentiles match 0 and 1. Background correction is done by over-smoothing an image and subtracting it from the original, then the red channel data are subtracted from the green, and, finally, each layer of the stack is filtered again (2D Gaussian, $\sigma = 2$ µm). The result is then searched for local maxima, with an adaptive threshold. If two selected locations are closer than a given distance threshold, only one is kept. At the end, the algorithm lists the 3D coordinates of the centers of each neuronal cell body, and these coordinates can be used during random-access scanning.

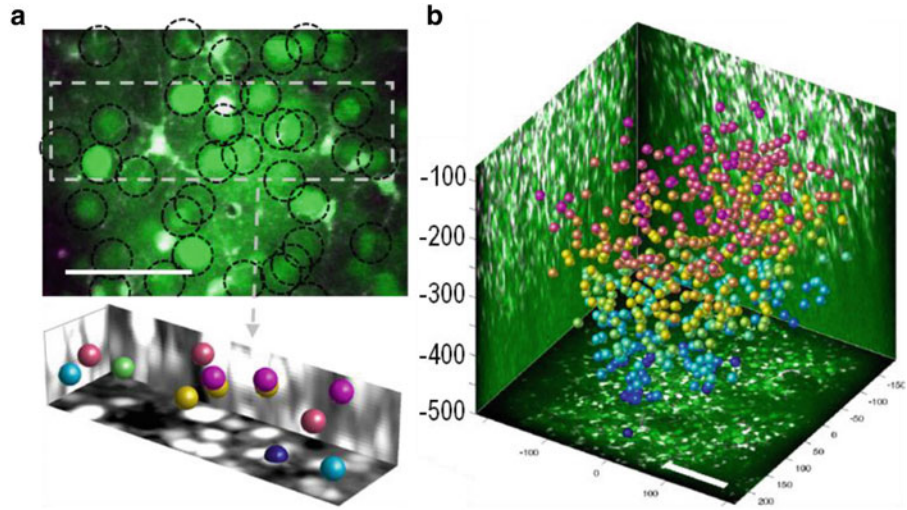

Fig. 21 Automatic localization of neurons in vivo. (**a**) 35 μm *z*-projection of a smaller region of the experiment shown in Fig. 20. *Bottom*, neuronal somata detected with the aid of an algorithm in a sub-volume (shown with projections, neurons in white and glial cells in *black*). Scale bar, 50 μm. (**b**) Maximal intensity side- and *z*-projections of the entire *z*-stack (400 × 400 × 500 μm^3) with autodetected cell locations. *Spheres* are color coded in relation to depth. The detection threshold used here yielded 532 neurons. Scale bar, 100 μm

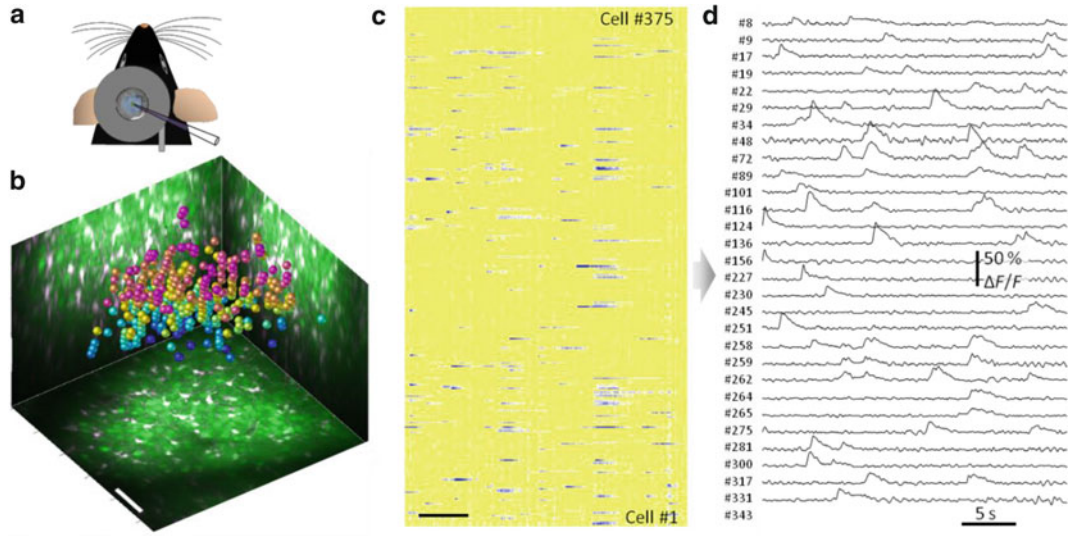

Fig. 22 Spontaneous neuronal network activity in vivo. (**a**) Sketch of in vivo experimental arrangement. (**b**) Maximal intensity side- and *z*-projection image of the entire *z*-stack (280 × 280 × 230 μm^3; bolus loading with OGB-1-AM and SR-101). *Spheres* represent 375 autodetected neuronal locations color coded by depth in the V1 region of the cortex. Scale bars, 50 μm. (**c**) Parallel 3D recording of spontaneous Ca^{2+} responses from the 375 locations. Rows, single cells measured in random-access scanning mode. Scale bar, 5 s. Activity was recorded with ~80 Hz. (**d**) Examples of Ca^{2+} transients showing active neurons from (**c**)

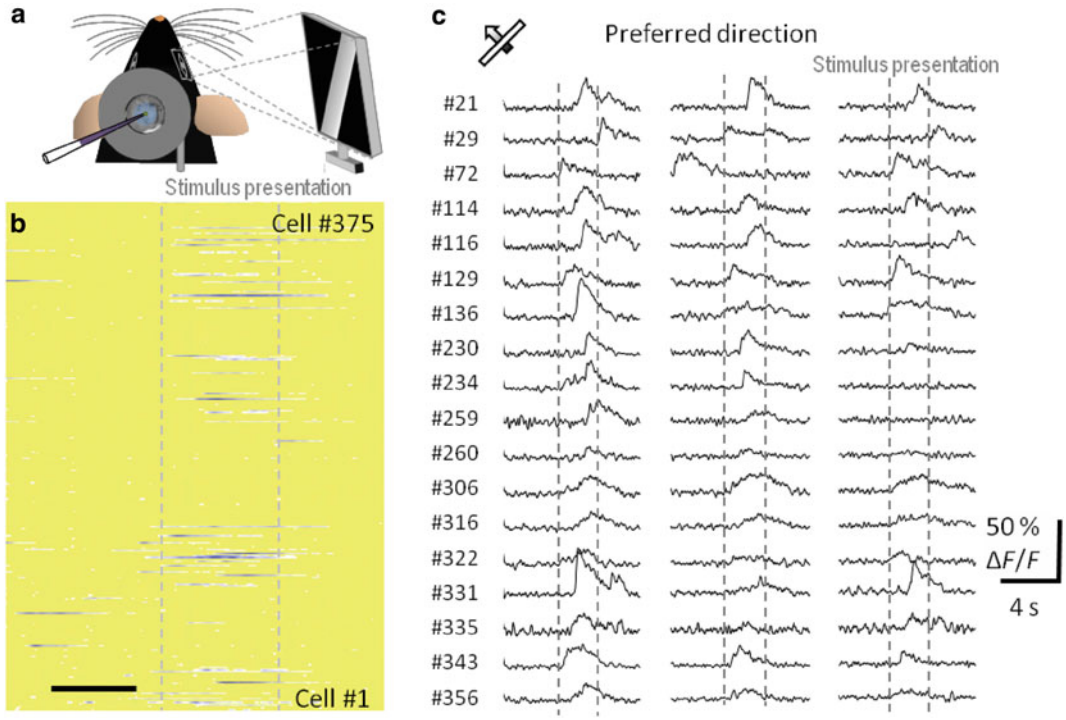

Fig. 23 Neuronal network activity in vivo in response to visual stimuli. (**a**) Sketch of in vivo experimental arrangement. Visual stimulation was induced by moving bars in eight directions at 45° intervals. (**b**) Ca^{2+} responses from the same 375 neuronal locations visible in Fig. 22 (visual stimulation: moving bar at −45°). Rows, single cells from a single 3D measurement. Scale bar, 2 s. (**c**) Examples of Ca^{2+} transients from neurons in **b**, preferentially responding to the −45° bar direction. Bar moved in the visual field during the time periods marked with *dashed lines*

After the selection of the cell bodies (Fig. 22b), the spontaneous activity of each neuron is recorded and the point-by-point background-corrected and normalized fluorescence data are plotted real-time. Data from each cell can also be shown as a single row or column for better visibility (Fig. 22c). The stability of long-term recording can be monitored by measuring the baseline fluorescence.

For neuroscientists, it is more interesting to record neuronal responses following different physiological stimulations in different cortical areas. For example, the mouse could be presented with visual stimuli consisting of movies of a white bar oriented at eight different angles and always moving perpendicular to its orientation (Fig. 23b) and detect responses in the V1 region of the cortex. Visual stimulation with bars oriented at −45° activate a small subpopulation of the measured cells (Fig. 23b and c).

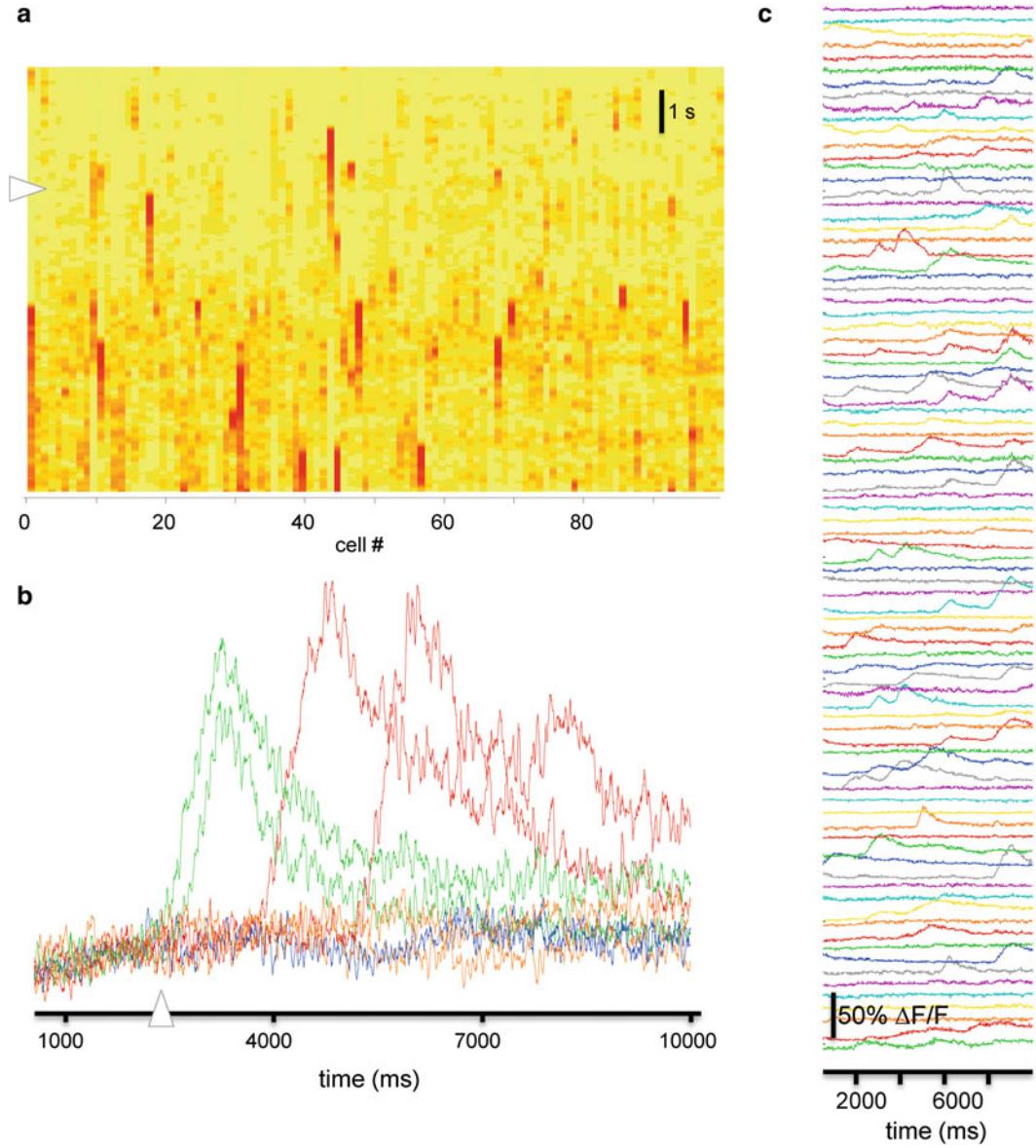

Fig. 24 Neuronal network activity recorded in the V1 region of an awake animal. (**a**) Spatially normalized 3D Ca^{2+} response recorded in 100 genetically labeled neurons. Each column corresponds to a single neuron. Red color indicates high activity. Neurons were labeled using AAV viruses and expressed GCamP6 sensor. (**b**) Exemplified Ca^{2+} responses, raw traces. (**c**) Simultaneously recorded population activity, each trace corresponds to a single neuron

4.4 In Vivo 3D Imaging of Genetically Labeled Neuronal Networks

Similarly to the measurements shown in the previous section, 3D recordings can also be performed on genetically labeled neuronal networks (Fig. 24). The improved capability of the recording technology is mostly because of the recent developments in the field of AOD scanner technology: the novel 3D scan heads provide better transmission, even at longer wavelengths.

5 Future Perspectives

Optically, 3D AO microscopes are now close to the theoretical maximum which can be realized using the currently available high NA objective lenses, but other aspects of AO scanning could still be improved, such as

- develop faster, more specialized scanning algorithms for network measurements
- develop faster AO deflectors
- develop novel correction methods for movement artifacts
- improve lasers and fluorescent dyes to get access to entire thickness of the cortex
- applying the technology to larger FOV objectives
- implement adaptive optics
- overcome the speed of resonant scanning in frame scanning modes
- simplify the system to lower its costs and maintenance efforts
- improve wavelength tunability

Together with these developments, there is a need for systems which can simultaneously scan multiple brain areas in order to study communication between sensory, motor, and higher order areas, and which are able to use photostimulation in combination with 3D scanning in order to map functional connectivity within neuronal networks. Moreover, 3D recordings must be performed in symbiosis with neuronal network and dendritic modeling; 3D recorded data must be explained by neuronal network and dendritic modeling; and, conversely, measurements must be performed according to modeling predictions [44, 46].

References

1. Johnston D, Narayanan R (2008) Active dendrites: colorful wings of the mysterious butterflies. Trends Neurosci 31(6):309–316
2. Katona G et al (2011) Roller Coaster Scanning reveals spontaneous triggering of dendritic spikes in CA1 interneurons. Proc Natl Acad Sci U S A 108(5):2148–2153
3. Losonczy A, Makara JK, Magee JC (2008) Compartmentalized dendritic plasticity and input feature storage in neurons. Nature 452 (7186):436–441
4. Spruston N (2008) Pyramidal neurons: dendritic structure and synaptic integration. Nat Rev Neurosci 9(3):206–221
5. Rozsa B et al (2008) Dendritic nicotinic receptors modulate backpropagating action potentials and long-term plasticity of interneurons. Eur J Neurosci 27(2):364–377
6. Rozsa B et al (2004) Distance-dependent scaling of calcium transients evoked by backpropagating spikes and synaptic activity in dendrites of hippocampal interneurons. J Neurosci 24 (3):661–670
7. Ohki K et al (2005) Functional imaging with cellular resolution reveals precise microarchitecture in visual cortex. Nature 433 (7026):597–603

8. Ariav G, Polsky A, Schiller J (2003) Submillisecond precision of the input-output transformation function mediated by fast sodium dendritic spikes in basal dendrites of CA1 pyramidal neurons. J Neurosci 23 (21):7750–7758
9. Danilatos GD (1991) Review and outline of environmental SEM at present. J Microsc 162 (3):391–402
10. Kherlopian AR et al (2008) A review of imaging techniques for systems biology. BMC Syst Biol 2:74
11. Kerr JN, Denk W (2008) Imaging in vivo: watching the brain in action. Nat Rev Neurosci 9(3):195–205
12. Amos WB, White JG, Fordham M (1987) Use of confocal imaging in the study of biological structures. Appl Opt 26 (16):3239–3243
13. Minsky M (1988) Memoir on inventing the confocal scanning microscope. Scanning 10 (4):128–138
14. Petráň M et al (1968) Tandem-scanning reflected-light microscope. J Opt Soc Am 58 (5):661–664
15. Tomer R et al (2012) Quantitative high-speed imaging of entire developing embryos with simultaneous multiview light-sheet microscopy. Nat Methods 9(7):755–763
16. Denk W, Strickler JH, Webb WW (1990) Two-photon laser scanning fluorescence microscopy. Science 248(4951):73–76
17. Denk W, Svoboda K (1997) Photon upmanship: why multiphoton imaging is more than a gimmick. Neuron 18(3):351–357
18. Goeppert-Mayer M (1931) Ueber Elementarakte mit zwei Quantenspruengen. Ann Phys 9:273
19. Helmchen F, Denk W (2005) Deep tissue two-photon microscopy. Nat Methods 2 (12):932–940
20. Kobat D, Horton NG, Xu C (2011) In vivo two-photon microscopy to 1.6-mm depth in mouse cortex. J Biomed Opt 16(10):106014
21. Theer P, Hasan MT, Denk W (2003) Two-photon imaging to a depth of 1000 micron in living brains by use of a Ti:Al_2O_3 regenerative amplifier. Opt Lett 28(12):1022–1024
22. Niesner R et al (2007) The power of single and multibeam two-photon microscopy for high-resolution and high-speed deep tissue and intravital imaging. Biophys J 93 (7):2519–2529
23. Prevedel R et al (2014) Simultaneous whole-animal 3D imaging of neuronal activity using light-field microscopy. Nat Methods 11 (7):727–730
24. Quirin S et al (2014) Simultaneous imaging of neural activity in three dimensions. Front Neural Circuits 8:29
25. Quirin S, Peterka DS, Yuste R (2013) Instantaneous three-dimensional sensing using spatial light modulator illumination with extended depth of field imaging. Opt Express 21(13):16007–16021
26. Grewe BF et al (2011) Fast two-layer two-photon imaging of neuronal cell populations using an electrically tunable lens. Biomed Opt Express 2(7):2035–2046
27. Nikolenko V et al (2008) SLM microscopy: scanless two-photon imaging and photostimulation with spatial light modulators. Front Neural Circuits 2:5
28. Gobel W, Kampa BM, Helmchen F (2007) Imaging cellular network dynamics in three dimensions using fast 3D laser scanning. Nat Methods 4(1):73–79
29. Cheng A et al (2011) Simultaneous two-photon calcium imaging at different depths with spatiotemporal multiplexing. Nat Methods 8(2):139–142
30. Holekamp TF, Turaga D, Holy TE (2008) Fast three-dimensional fluorescence imaging of activity in neural populations by objective-coupled planar illumination microscopy. Neuron 57(5):661–672
31. Botcherby EJ et al (2012) Aberration-free three-dimensional multiphoton imaging of neuronal activity at kHz rates. Proc Natl Acad Sci U S A 109(8):2919–2924
32. Rozsa B et al (2007) Random access three-dimensional two-photon microscopy. Appl Opt 46(10):1860–1865
33. Katona G et al (2012) Fast two-photon in vivo imaging with three-dimensional random-access scanning in large tissue volumes. Nat Methods 9(2):201–208
34. Kaplan A, Friedman N, Davidson N (2001) Acousto-optic lens with very fast focus scanning. Opt Lett 26(14):1078–1080
35. Fernandez-Alfonso T et al (2014) Monitoring synaptic and neuronal activity in 3D with synthetic and genetic indicators using a compact acousto-optic lens two-photon microscope. J Neurosci Methods 222:69–81
36. Cotton RJ et al (2013) Three-dimensional mapping of microcircuit correlation structure. Front Neural Circuits 7:151
37. Kirkby PA, Srinivas Nadella KM, Silver RA (2010) A compact acousto-optic lens for 2D and 3D femtosecond based 2-photon microscopy. Opt Express 18(13):13721–13745
38. Duemani Reddy G et al (2008) Three-dimensional random access multiphoton

microscopy for functional imaging of neuronal activity. Nat Neurosci 11(6):713–720

39. Iyer V, Hoogland TM, Saggau P (2006) Fast functional imaging of single neurons using random-access multiphoton (RAMP) microscopy. J Neurophysiol 95(1):535–545
40. Reddy GD, Saggau P (2005) Fast three-dimensional laser scanning scheme using acousto-optic deflectors. J Biomed Opt 10 (6):064038
41. Grewe BF et al (2010) High-speed in vivo calcium imaging reveals neuronal network activity with near-millisecond precision. Nat Methods 7(5):399–405
42. Proctor B, Wise F (1992) Quartz prism sequence for reduction of cubic phase in a mode-locked Ti:Al(2)O(3) laser. Opt Lett 17 (18):1295–1297
43. Keren N, Bar-Yehuda D, Korngreen A (2009) Experimentally guided modelling of dendritic excitability in rat neocortical pyramidal neurones. J Physiol 587(Pt 7):1413–1437
44. Almog M, Korngreen A (2014) A quantitative description of dendritic conductances and its application to dendritic excitation in layer 5 pyramidal neurons. J Neurosci 34(1):182–196
45. Nimmerjahn A et al (2004) Sulforhodamine 101 as a specific marker of astroglia in the neocortex in vivo. Nat Methods 1(1):31–37
46. Chiovini B et al (2014) Dendritic spikes induce ripples in parvalbumin interneurons during hippocampal sharp waves. Neuron 82(4):908–924